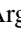# Effect of centrality selection on higher-order cumulants of net-proton multiplicity distributions in relativistic heavy-ion collisions

Arghya Chatterjee [1], Yu Zhang [1], Jingdong Zeng,[1] Nihar Ranjan Sahoo [2], and Xiaofeng Luo [1,*]

[1]*Key Laboratory of Quark & Lepton Physics (MOE) and Institute of Particle Physics, Central China Normal University, Wuhan 430079, China*
[2]*Shandong University, Qingdao, Shandong 266237, China*

We studied the centrality selection effect on cumulants (up to fourth order) and the cumulants' ratios of net-proton multiplicity distributions in Au + Au collisions at $\sqrt{s_{NN}} = 7.7$, 19.6, and 200 GeV from the ultrarelativistic quantum molecular dynamic model. The net-proton cumulants were calculated with collision centralities by using charged-particle multiplicity from different pesudorapidity (η) regions. By comparing the results from various collision centralities, we found that the autocorrelation effects are not significant in the results with the collision centralities "refmult-3" and "refmult-2," which use midrapidity charged particles but exclude (anti)protons and the analysis region, respectively. Furthermore, due to the contributions of spectator protons, we observed poor centrality resolution when using charged particles at forward η regions at low energies. This work can serve as a baseline for centrality selection of future fluctuations analysis in relativistic heavy-ion collisions.

I. INTRODUCTION

One of the major goals of high-energy heavy-ion collision experiments is to explore the phase structure of the strongly interacting QCD matter [1]. The QCD phase structure can be represented as a function of temperature (T) and baryon chemical potential (μ_B) [2]. QCD-based model calculations predict that at large μ_B the transition from hadronic matter to quark-gluon plasma (QGP) is of first order [3,4]. The end point of the first-order phase transition boundary is known as the QCD critical point (CP), after which there is no genuine phase transition but a smooth crossover from hadronic to quark-gluon degrees of freedom [5,6]. Many efforts have been made to find the signature and/or location of the CP, theoretically [7–18] and experimentally [19]. However, the location of the CP and even the existence of the CP have not been confirmed yet. Experimental confirmation of the existence of the critical point will be a milestone for the study of QCD phase structure.

One of the foremost methods for the critical point search is through measuring the event-by-event higher-order fluctuations (called "cumulants") of conserved quantities, such as net-charge (Q), net-baryon (B), and net-strangeness (S), because of their divergence nature near the critical point [20,21]. Due to the limitation of measuring neutral particles, experimentally we measured the cumulants of net proton and net kaon as a proxy of net baryon and net strangeness, respectively. The STAR experiment at the BNL Relativisitic Heavy Ion Collider (RHIC), over past few years have measured the higher order cumulants up to forth order of net-

proton [22–25], net-charge [26] and net-kaon [27] multiplicity distributions. Recently the STAR Collaboration has also reported the cross cumulants between net particles [28]. Theoretically nth order cumulants are related to the nth order thermodynamic susceptibilities as $C_n = VT^3\chi_n$, where V and T are the system volume and temperature, respectively. To compare the experimental measurements with theoretical susceptibilities, different cumulant ratios are constructed (like, $C_2/C_1 = \chi_2/\chi_1$, $C_3/C_2 = \chi_2/\chi_1$, and $C_4/C_2 = \chi_4/\chi_2$, etc.). Cumulant values are also related with the correlation length (ξ) of the matter created in the collisions as $\sigma^2 = C_2 = \xi^2$, $S = C_3/C_2^{3/2} = \xi^{4.5}$, and $\kappa = C_4/C_2^2 = \xi^7$ [29,30]. One of the characteristic signatures of the QCD CP is the divergence of correlation length, which gives a nonmonotonic variation of these cumulant ratios as a function of μ_B. The STAR experiment at RHIC has measured the cumulant ratios of net-proton, net-charge, and net-kaon multiplicity distributions in Au + Au collisions at a broad range of collision energies from 200 GeV down to 7.7 GeV, which correspond to a chemical freeze-out μ_B range from 20 to 420 MeV. Interestingly, the forth-order net-proton cumulant ratio ($\kappa\sigma^2 = C_4/C_2$) for most central 0–5% collisions shows a nonmonotonic variation as a function of collision energy [24].

To understand the underlying physics associated with this measurement, we need to perform careful studies on the background contributions, such as the effects from initial volume fluctuations, the detector efficiency, and the effects of centrality selection. Some of the effects have been discussed before [31–36]. Collision centralities can be quantified by the impact parameter (b) or the number of participant nucleons (N_{part}). Unfortunately, in experiments we cannot directly measure such geometrical variables. As the particle multiplicities depend on the initial geometry, so the collision

centrality in heavy-ion collisions is usually determined by the charged-particle multiplicities. The centrality resolution is determined by the multiplicities and kinematics of the charged particles used in the centrality definition. As the bad centrality resolution will introduce larger volume fluctuations and enhance the higher-order cumulants, a good centrality resolution of the charged-particle centrality definition is very important for fluctuation analysis. On the other hand, there is the so-called autocorrelation effect [31], which indicates that values of higher-order cumulants will be suppressed if the charged particles involved in the centrality definition are also used in the cumulant calculations. To avoid the autocorrelation, particles from different kinematic regions are proposed to define the collision centralities. Experimentally, a dedicated event plane detector (EPD) [37] has been built and installed in the forward region ($2.1 < |\eta| < 5.1$) of the STAR experiment. The EPD will be used for event plane and centrality determination in the second phase of the Beam Energy Scan program (BES-II,2019-2021) at RHIC. It has been proposed that the centrality selection by using the EPD will strongly suppress the effect of autocorrelation in the fluctuation analysis [38]. In this work, we demonstrate the variation of net-proton cumulant values by selecting centralities from different central regions as well as the forward region using the ultrarelativistic quantum molecular dynamic (UrQMD) model.

The paper is organized as follows. In Sec II, we briefly discuss the UrQMD model used for this analysis. In Sec. III, we introduce the observables presented here. The centrality selection is discussed in Sec. IV. In Sec. V, we present cumulants (C_1–C_4) of the net-proton multiplicity distributions for different centrality definitions in Au + Au collisions at $\sqrt{s_{NN}} = 7.7$, 19.6, and 200 GeV using the UrQMD model. Finally in Sec. VI, we present a summary of this work.

II. THE URQMD MODEL

The UrQMD model is a microscopic transport model [39,40]. In this model, the space-time evolution of the fireball is studied in terms of excitation of color strings that fragment further into hadrons, the covariant propagation of hadrons and resonances that undergo scatterings, and finally the decay of all the resonances. The UrQMD model has been quit successful and widely applied towards heavy-ion phenomenology [40,41]. Previously, this model has been used to compute several cumulants and to study different effects of experimental limitations [31,32,42–48]. The choice of acceptance window plays an important role in such studies. The initial distributions of the net-baryon number (N_B) in rapidity is a consequence of the baryon stopping phenomenon, which strongly depends on the collision energy. As a result, the midrapidity region for high $\sqrt{s_{NN}}$ is free of N_B while at lower $\sqrt{s_{NN}}$ most of the N_B are deposited in the midrapidity region. This collision-energy-dependent baryon stopping phenomenon is dynamically included in the UrQMD model. More details about the UrQMD model can be found in Refs. [39,40]. In this study, we have used six million events per beam energy for Au + Au collisions at $\sqrt{s_{NN}} = 7.7$, 19.6, and 200 GeV. Using these simulated events, we measure the cumulants of event-by-event net-proton ($N_{p-\bar{p}}$) multiplicity

distributions within the kinematic acceptance $|y| < 0.5$ and $0.4 < p_T < 2.0$ GeV/c . The same kinematic acceptance has been used in the net-proton cumulant analysis by the STAR experiment [24].

III. OBSERVABLES

In statistics, any distribution can be characterized by different order moments or cumulants (C_n) and can be expressed via the generating function [49] as

$$C_n = \frac{\partial^n}{\partial \alpha^n} K(\alpha)|_{\alpha=0}, \qquad (1)$$

where $K(\alpha) = \ln[M(\alpha)]$ and $M(\alpha) = \langle e^{\alpha N} \rangle$ are the cumulant and moment generating functions, respectively. N is the event-by-event net-quantity (here the net-proton number, $N_p = N_p - N_{\bar{p}}$) and $\langle \cdots \rangle$ represents an average over events. Then the various order cumulants can be expressed as

$$C_1 = \langle N \rangle, \qquad (2)$$

$$C_2 = \langle (\delta N)^2 \rangle, \qquad (3)$$

$$C_3 = \langle (\delta N)^3 \rangle, \qquad (4)$$

$$C_4 = \langle (\delta N)^4 \rangle - 3 \langle (\delta N)^2 \rangle, \qquad (5)$$

where $\delta N = N - \langle N \rangle$ represents the deviation of N from its average value. $\langle (\delta N)^m \rangle$ is also called the mth-order central moment. Thermodynamically the cumulants are connected to the corresponding susceptibilities by

$$C_n = \frac{\partial^n \ln[Z(V, T, \mu)]}{\partial \mu^n} = V T^3 \chi_n. \qquad (6)$$

The cumulant ratios between different orders can be constructed to cancel the volume term. The cumulant ratios are measured experimentally and compared to the susceptibility ratios [19,50]:

$$\frac{\sigma^2}{M} = \frac{C_2}{C_1} = \frac{\chi_2}{\chi_1}, \quad S\sigma = \frac{C_3}{C_2} = \frac{\chi_3}{\chi_2}, \quad \kappa\sigma^2 = \frac{C_4}{C_2} = \frac{\chi_4}{\chi_2}. \qquad (7)$$

With the above definitions, we have studied various cumulants (up to forth order) and cumulant ratios of event-by-event net-proton multiplicity distributions from the UrQMD model with different centrality selections.

In heavy-ion collisions, we cannot directly measure the geometrical variables, such as impact parameter. The collision centrality in heavy-ion collisions is usually determined through charged-particle multiplicities, in which the smallest centrality bin is a single multiplicity value. However, for better statistical significance, we report the cumulant results for wider centrality bins, like 0–5% (most central) or 70–80% (peripheral). But, these particle multiplicities not only reflect the initial geometry but also depend on different physics processes. This also shows that the measured observables N_{ch} and the geometrical variable (b) are not one-to-one correspondences. A fixed N_{ch} may come from different initial geometries. This variation even becomes large when we use a wider 5% or 10% centrality class. To reduced the variation for wider centrality bins, a so-called centrality bin width
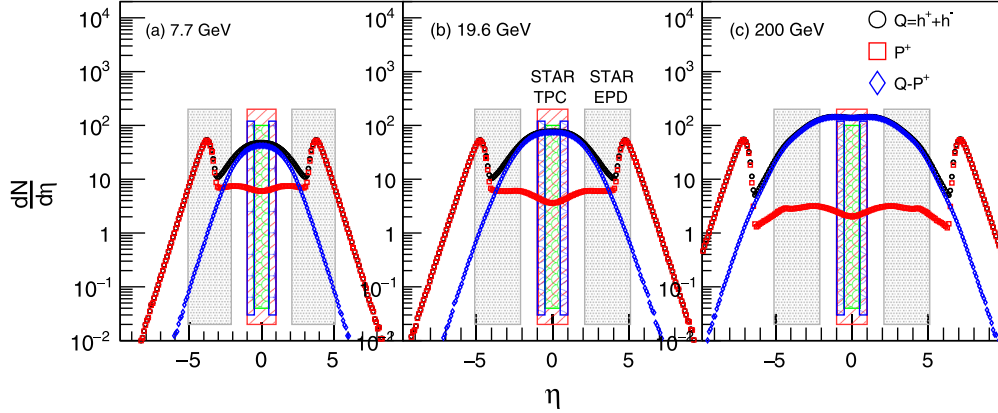
FIG. 1. The $dN/d\eta$ distributions for charged-particle, proton, and $N_{\mathrm{ch}} - p$ multiplicities in Au + Au collisions at $\sqrt{s_{NN}} = 7.7$, 19.6, and 200 GeV. The bands of different colors correspond to different pseudorapidity (η) regions for the centrality selection.

correction (CBWC) technique is applied in cumulant analysis [31]. The techniques for this correction are as follows. We first calculate different cumulants (C_n) in each bin of unit multiplicity and then weight the cumulants by the number of events in each bin over a desired centrality class. The method can be expressed as

$$C_n = \frac{\sum_i n_i C_{n_i}}{\sum_i n_i} = \sum_i \omega_i C_{n_i}, \qquad (8)$$

where C_{n_i} is the cumulant value measured in the ith multiplicity bin. n_i and $\omega_i (= n_i / \sum_i n_i)$ are the number of events and the weight factor for the ith multiplicity bin. It was shown that the CBWC can effectively suppress the volume fluctuations within a wide centrality bin [31]. However, even when the CBWC is applied, there could be still residual volume fluctuations if the centrality resolution is not good. Another centrality-selection-related artifact is the so-called autocorrelation effect, which is due to the correlations between particles used in the centrality selection and the cumulant calculations. For example, a typical autocorrelation effect is caused by the fact that some of the particles involved in the cumulant analysis are also used for the centrality selection. In the STAR experiment, to avoid the autocorrelation effect in net-proton and net-charge fluctuation measurements, collision centralities are carefully selected, the so-called "refmult-3" and "refmult-2," respectively. In the refmult-3 definition, the collision centrality is determined by the measured charged-particle multiplicities (N_{ch}) within $|\eta| < 1.0$ excluding protons and antiprotons, while the refmult-2 centrality is defined by the measured charged particles within $0.5 < |\eta| < 1.0$. In BES-II, a dedicated forward EPD with coverage $2.1 < |\eta| < 5.1$ will be installed at the STAR experiment. The EPD will collect the ionization signals of charged particles and allow us to define the collision centrality in the forward rapidity region (like EPD region in STAR) instead of midrapidity region [38]. We demonstrate the effects of autocorrelations by selecting centralities from different region and discuss the effects of the spectator protons in the centrality selection with forward charged particles.

Figure 1 shows the pseudorapidity (η) distributions ($dN/d\eta$) of charged-particle, proton (p), and $N_{\mathrm{ch}} - p$ multiplicities for the minimum-bias Au + Au collisions at $\sqrt{s_{NN}} = 7.7$, 19.6, and 200 GeV. The bands at different η regions correspond to the acceptance of the STAR time projection chamber (TPC) and the EPD, respectively. The particle pseudorapidity (η) distribution is not uniform throughout the acceptance for all energies. At the forward pseudorapidity region from 2 to 5 units, one can find lots of spectator contributions at low energies. We can see two peak structures around $|\eta| = 7$–8 for 200 GeV, which correspond to the spectator protons. As we go towards low beam energies, the peaks shift towards the central η region; for example, for 7.7 GeV the peak is around $|\eta| = 3.5$. For the η window from 2.1 to 5.1 units at 200 GeV, the charged particles are mostly contributed from the produced particles. However, if we go towards lower beam energies, charged particles in that range are dominated by spectator protons, because most of the spectator protons are around beam rapidity.

Figure 2 shows the beam rapidity for different center-of-mass energies and the corresponding η values at $p_T = 0.2$ GeV/c. We found that at low energies between 3 and 27 GeV, the protons with beam rapidity and $p_T = 0.2$ GeV/c fall into the η coverage of the STAR EPD ($2.1 < |\eta| < 5.1$), which also leaves ionization signals in the EPD as other produced charge particles. Due to lack of particle identification capability of the EPD, we has difficulty isolating the signals of spectator protons, especially at low energies. The contamination of the spectator protons distorts the correlations between the charged particle signals and the collision centrality. Consequently, the collision centrality determined from the EPD has poor resolution, which enhances the volume fluctuations within a centrality bin. In the following, we demonstrate the effect of the spectator protons on the centrality selection and the net-proton cumulant analysis.

IV. CENTRALITY SELECTION

In this work we select centralities using charged-particle multiplicities from different η regions. The definitions of different centrality selections are listed in Table I. We further
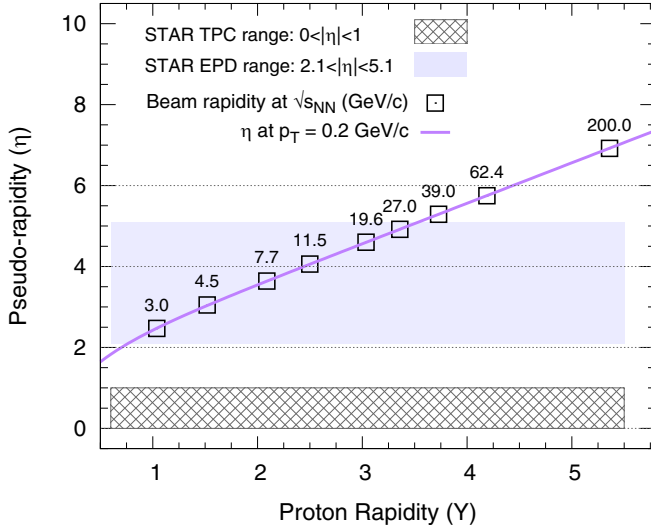
FIG. 2. Beam rapidity values as a function of center-of-mass energy. Central and forward detector regions for the centrality selection using charged-particle multiplicity are represented in black and blue band, respectively. The relation of p_T, pseudorapidity (η), and rapidity (y) is $p_T = m_0/\sqrt{\sinh^2\eta/\sinh^2 y - 1}$, where m_0 is the particle rest mass.

subdivide the forward region "Fwd-All" range into three regions: (a) Fwd-1, pseudorapidity acceptance $2.1 < |\eta| < 3$; (b) Fwd-2, within $3 < |\eta| < 4$; and (c) Fwd-3, within $4 < |\eta| < 5$. Figure 3 shows the minimum-bias charged-particle multiplicity distributions at $\sqrt{s_{NN}} = 7.7$, 19.6, and 200 GeV from different acceptance regions as listed in Table I. We selected nine different centrality classes: 0–5% (top central), 5–10%, 10–20%, 20–30%, 30–40%, 40–50%, 50–60%, 60–70%, and 70–80% from the area percentile of the multiplicity distributions. We find that at $\sqrt{s_{NN}} = 7.7$ and 19.6 GeV the multiplicity distributions at the forward region behave differently than those at the central region. This is mainly caused by the spectator protons, which are positively correlated with the impact parameter and are opposite to the trend of the produced charged-particle multiplicity distributions. As shown in Fig. 3, if we exclude the protons from the forward region, then the trend of the distributions looks like a hose-tail shaped similar to the central ones.

TABLE I. Definitions of different centrality selection methods used in this work.

Identify	Definition
centrality-b	Impact parameter
refmult-1	N_{ch} within $|\eta| < 0.5$
refmult-2	N_{ch} within $0.5 < |\eta| < 1.0$
refmult-3	$N_{ch} - p$ within $|\eta| < 1.0$
Fwd-All	N_{ch} within $2.1 < |\eta| < 5.1$
Fwd-1	N_{ch} within $2.1 < |\eta| < 3.0$
Fwd-2	N_{ch} within $3.0 < |\eta| < 4.0$
Fwd-3	N_{ch} within $4.0 < |\eta| < 5.0$
Fwd-All $- p$	$N_{ch} - p$ within $2.1 < |\eta| < 5.1$

Figure 4 shows the two-dimensional correlation plots between the charged-particle multiplicity distributions in different acceptance and the impact parameter. It was found that at lower energies the multiplicities within $2.1 < |\eta| < 5.1$ are positively correlated with the impact parameter; i.e., we get more particles in peripheral collisions than in central collisions, which are mainly contributed from the spectator protons. Figure 5 shows the impact parameter distributions for three different centrality classes in Au + Au collisions at $\sqrt{s_{NN}} = 7.7$, 19.6, and 200 GeV using different centrality definitions. To compare the centrality resolution between different centrality definitions, we define the quantity $\Phi (= \sigma_{b_X}^2/\sigma_{b_{\text{centrality-b}}}^2)$ as shown in Fig. 6, where the "X" is different centrality definitions using N_{ch} as discussed before. Here, $\sigma_{b_X}^2$ is the variance in impact parameter distribution in a centrality class from "X" centrality definition, whereas $\sigma_{b_{\text{centrality-b}}}^2$ represents the variance in impact parameter distribution with the centrality defined by the impact parameter (b) itself. So larger values in Φ correspond to a poorer resolution than smaller Φ values.

We find that the resolution in the refmult-3 definition is better for all energies, followed by refmult-2 and refmult-1. At $\sqrt{s_{NN}} = 7.7$ and 19.6 GeV, the resolution becomes poorer as we go towards the larger η region. This is due to the spectator contributions. It is also observed that the resolution is improved if we select centrality from the forward region by excluding protons. Still the Φ value is large at 7.7 GeV because of the smaller number of produced particles in that region. We can also observe that the centrality resolutions in central collisions are always better than those in peripheral collisions.

V. RESULTS

In this study, we compare the cumulants and their ratios of event-by-event net-proton multiplicity distributions within the kinematic acceptance $|y| < 0.5$ and $0.4 < p_T < 2.0$ GeV/c for different centrality definitions as discussed in the previous section. Figure 7 shows the event-by-event net-proton multiplicity distributions for Au + Au collisions at $\sqrt{s_{NN}} = 7.7$, 19.6, and 200 GeV for three centralities (0–5%, 30–40%, and 60–70%). We can find that the mean and the width for central collisions are larger than those for peripheral collisions. The mean values of net-proton distributions shift towards zero as the energy increases. At 200 GeV, the net-proton distributions from all the centrality sets are very similar. At 7.7 GeV, the net-proton distributions for the Fwd-All centrality case looks completely different. This is mainly caused by the distortion of the spectator protons in the centrality definition Fwd-All. As shown in Fig. 5, due to the positive correlations between the number of spectator protons and the impact parameter, the impact parameter distribution from Fwd-All contains more peripheral events (large b values) in the 0–5% centrality class than in the 60–70% centrality class. One needs to keep in mind that the raw net-proton distributions shown in Fig. 7 are not directly used to calculate various order cumulants, and one needs to apply the CBWC to suppress volume fluctuations in a wide centrality bin.
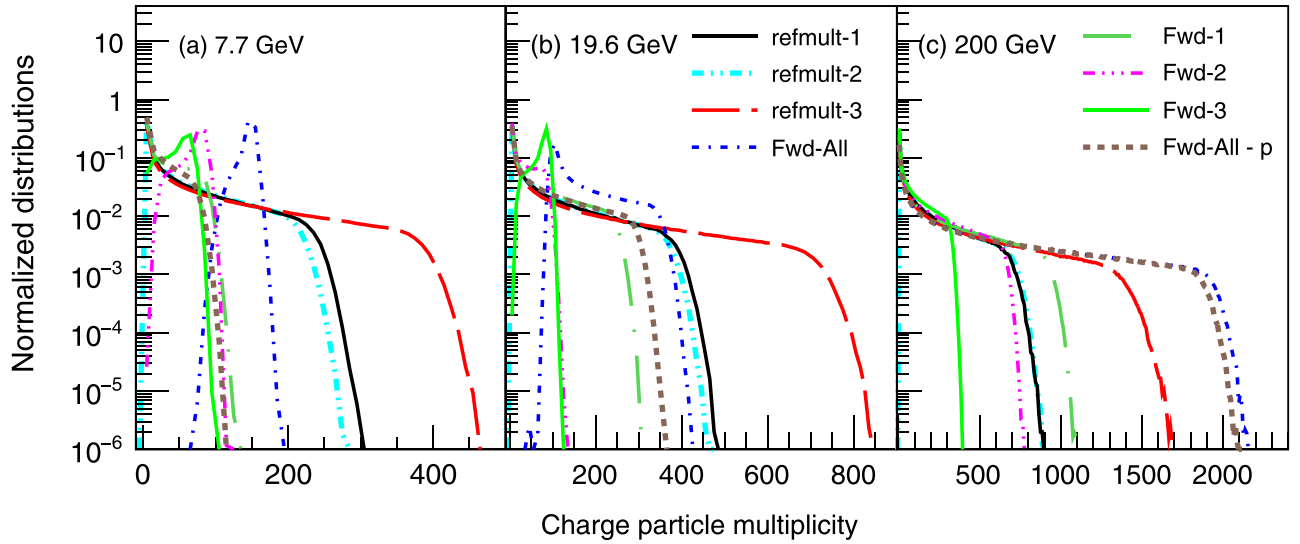
FIG. 3. Normalized distributions for charged-particle multiplicities in different η windows in Au + Au collisions at $\sqrt{s_{NN}}$ = 7.7, 19.6, and 200 from the UrQMD model.

Figure 8 shows the centrality dependence of cumulants (C_1 to C_4) of net-proton multiplicity distributions in Au + Au collisions at $\sqrt{s_{NN}}$ = 7.7, 19.6, and 200 GeV. The collision centralities are represented by the average number of participant nucleons ($\langle N_{part} \rangle$). We use a Monte Carlo Glauber model [51,52] to estimate N_{part} similarly to conventional cumulant analysis [22–24,26–28]. The statistical uncertainties are obtained using the analytical error propagation method [53–55]. The statistical uncertainties mainly depend on the variance of the respective distributions and the number of events. All the cumulants show a linear dependence as a function of $\langle N_{part} \rangle$. However C_1 and C_2 at $\sqrt{s_{NN}}$ = 7.7 GeV show an opposite trend for the Fwd-All centrality case. This is because at 7.7 GeV within 2.1 < $|\eta|$ < 5.1 most of the

charged particles are spectator protons. So in this region, larger N_{ch} percentiles correspond to peripheral collisions not central collisions. However, if we substract protons from the Fwd-All centrality definitions, then C_1 matches to other cases. We also observe that the cumulants values based on the refmult-2 and refmult-3 centrality definitions are consistent for all three energies. For lower beam energies ($\sqrt{s_{NN}}$ = 7.7 and 19.6 GeV) higher-order cumulants (C_3 and C_4) from the Fwd-All and Fwd-All-p centrality definitions deviate from the cumulants using the refmult-2 and refmult-3 centrality definitions. This is because of the poor centrality resolution in the Fwd-All and Fwd-All-p centrality definitions due to smaller multiplicity distributions and/or spectator contributions. For $\sqrt{s_{NN}}$ = 19.6 GeV, we found the values of
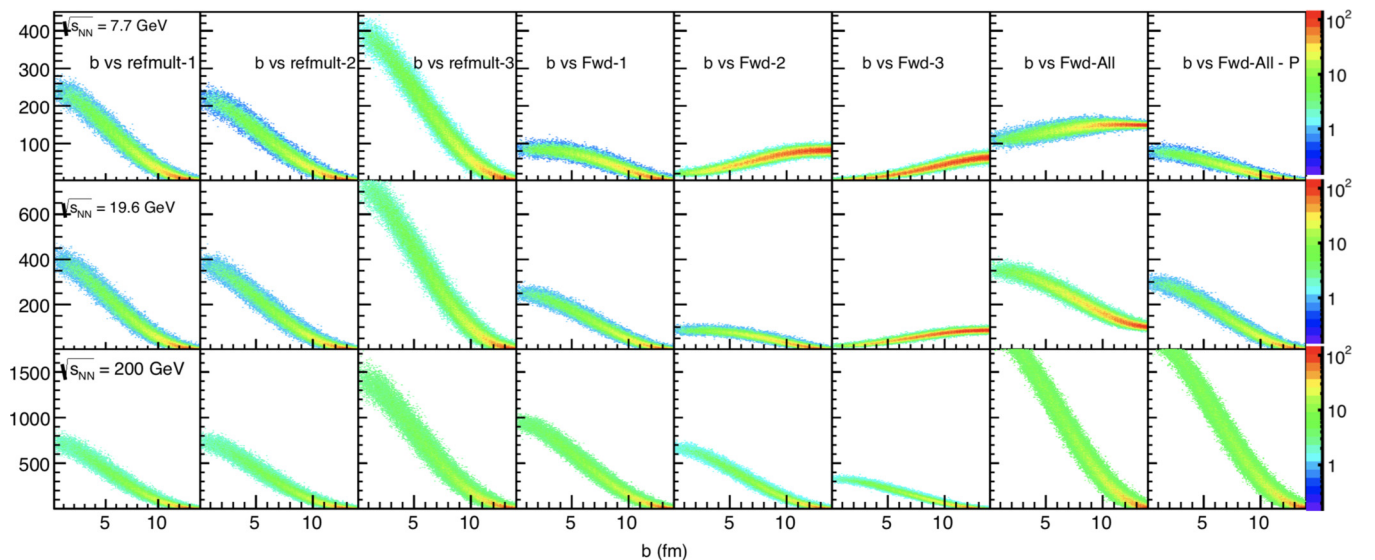

FIG. 4. Correlations between multiplicities in different η windows used for the centrality definitions and impact parameters in Au + Au collisions at $\sqrt{s_{NN}}$ = 7.7, 19.6, and 200 GeV from the UrQMD model.
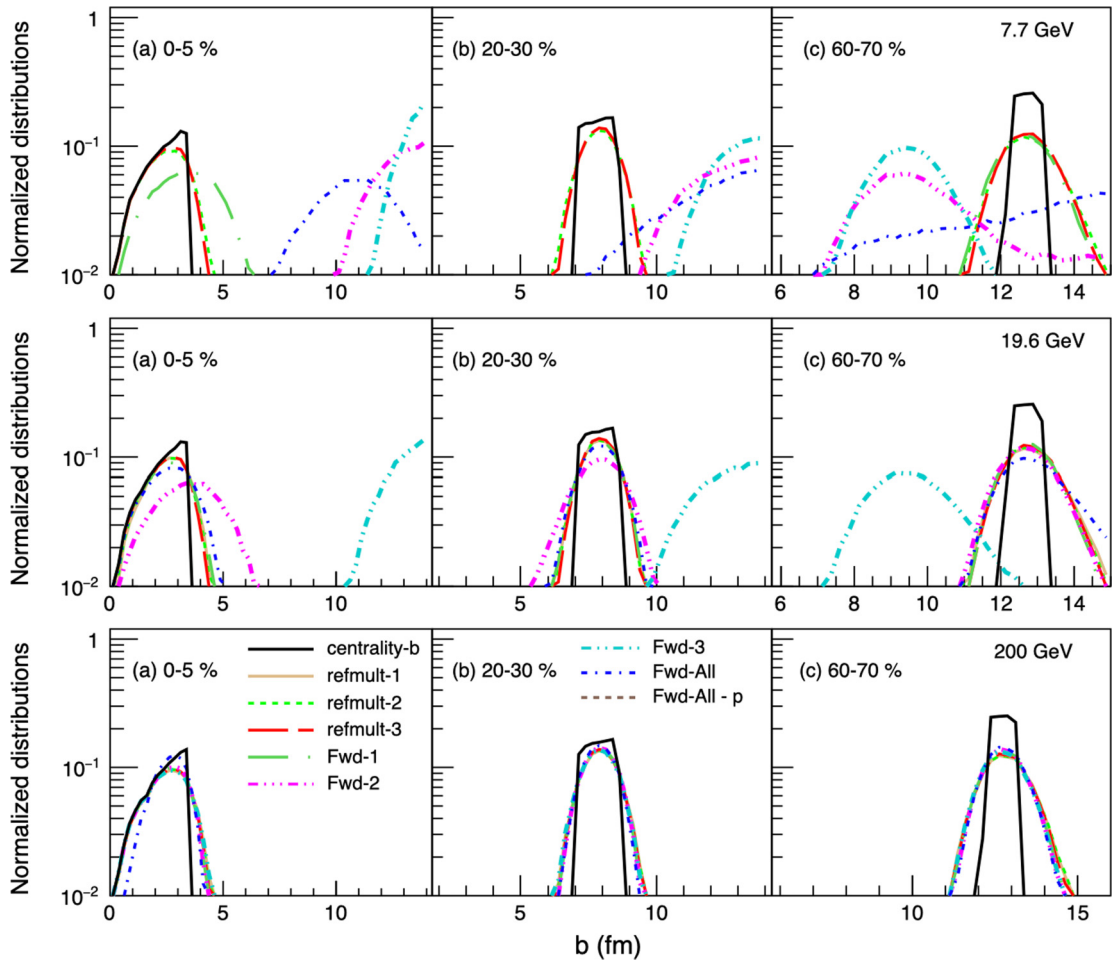
FIG. 5. The impact parameter (b) distributions in different centrality definitions for three different centrality classes [(a) 0–5%, (b) 20–30%, and (c) 60–70%] at $\sqrt{s_{NN}} = 7.7$, 19.6, and 200 GeV.

higher-order cumulants from refmult-1 are smaller than the results from the Fwd-All-p centrality definition. This is caused by the autocorrelation effect in the refmult-1 centrality defini-

tion, because the centrality resolution of Fwd-All-p is better than that in the case of refmult-1. Meanwhile, at 19.6 GeV, we found the higher-order cumulants from the refmult-2 and
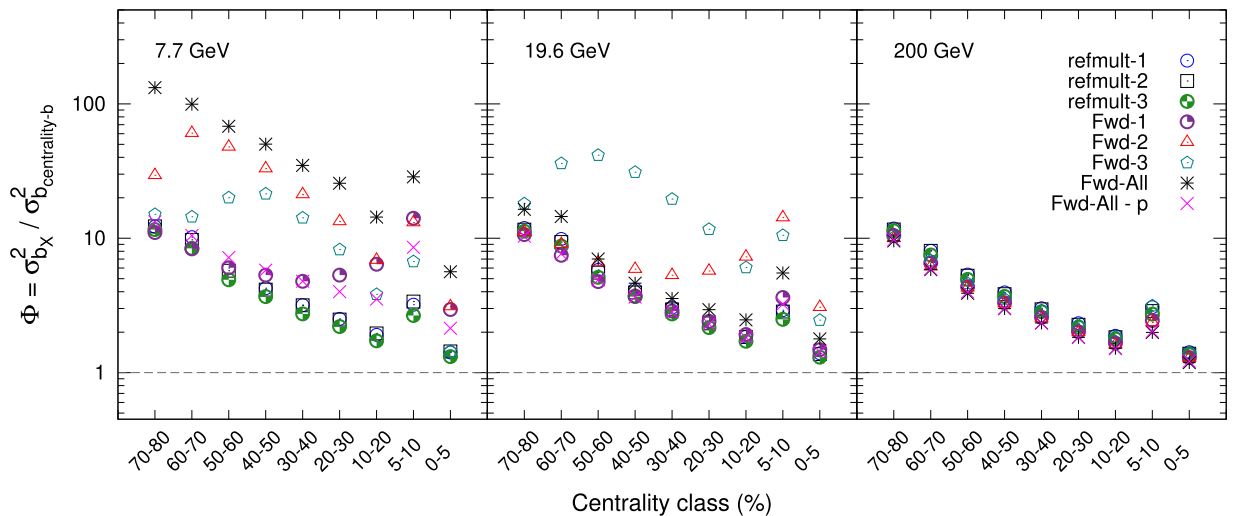
FIG. 6. The centrality dependence of $\Phi(=\sigma_{b_X}^2/\sigma_{b_{centrality-b}}^2)$ of impact parameter distributions for Au + Au collisions at $\sqrt{s_{NN}} = 7.7$, 19.6, and 200 GeV in the UrQMD model with different centrality definitions.
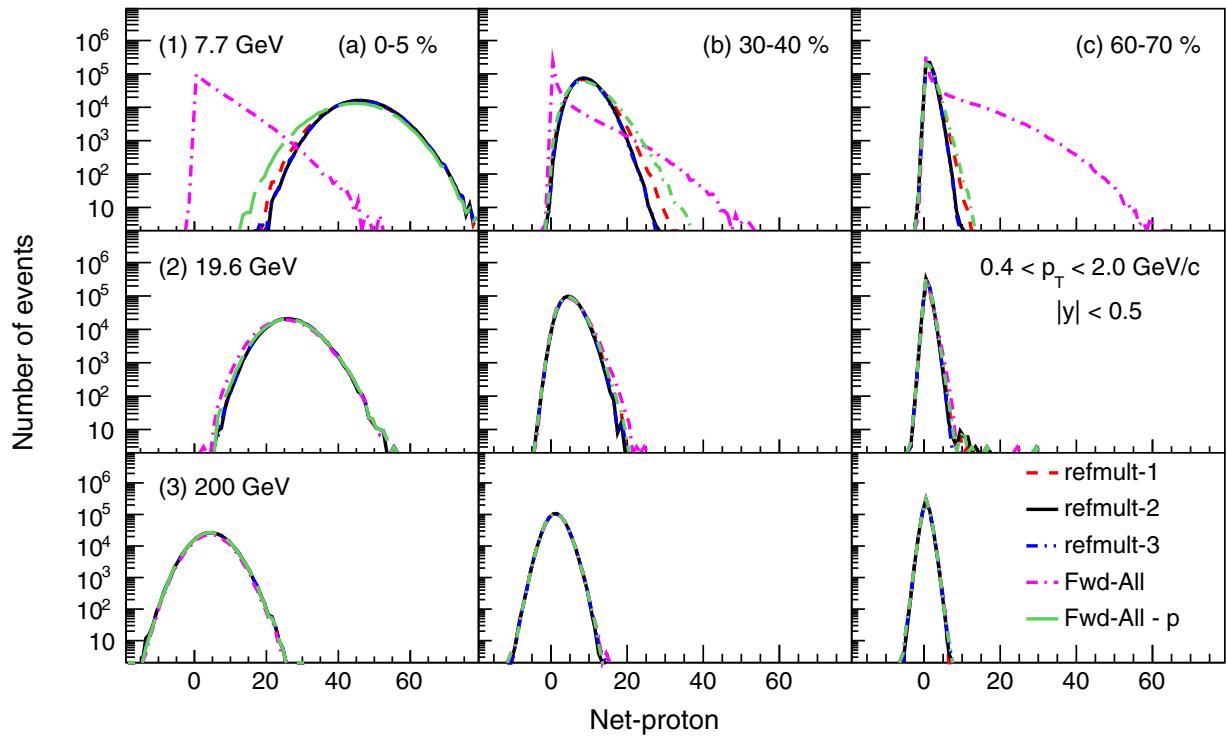
FIG. 7. Event-by-event distributions of net-proton multiplicity distributions for Au + Au collisions at $\sqrt{s_{NN}}$ = 7.7, 19.6, and 200 GeV for different centrality selection methods.
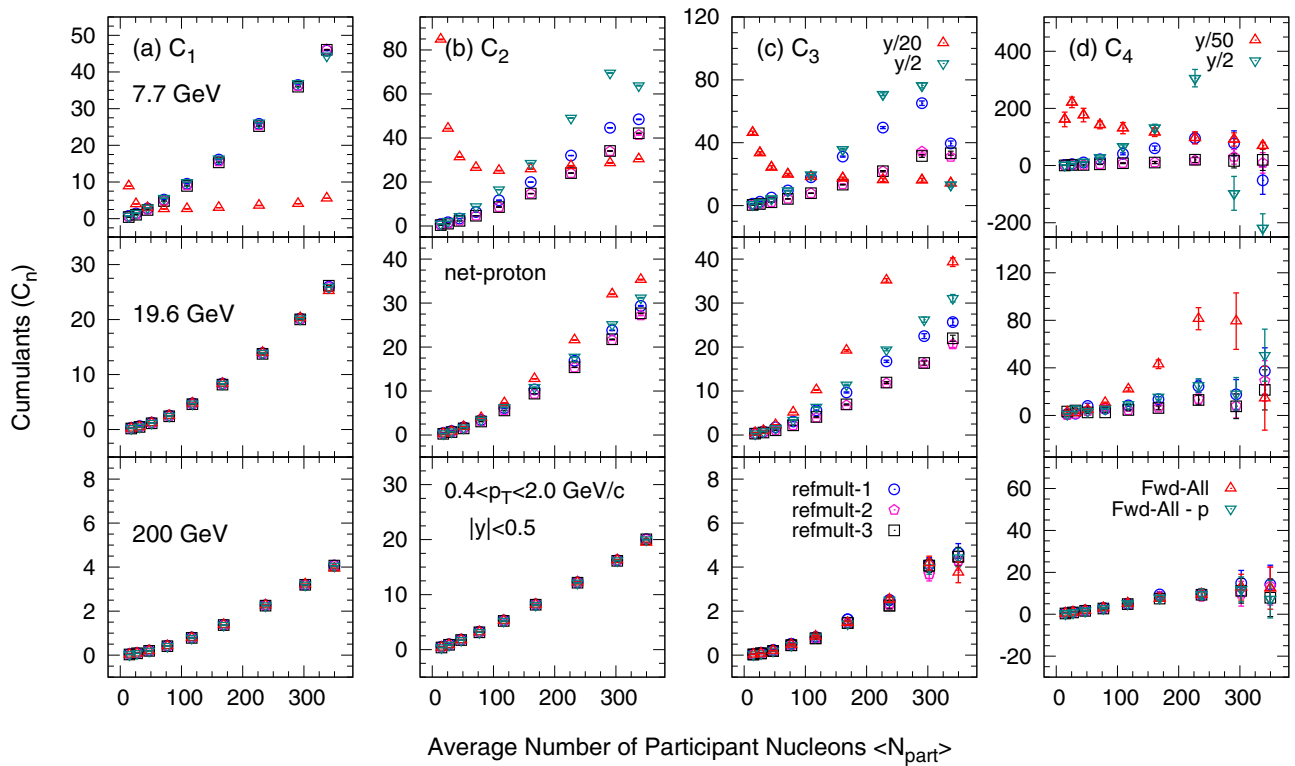

FIG. 8. Centrality dependence of cumulants (C_1–C_4) of net-proton multiplicity distributions within $|y| < 0.5$ and $0.4 < p_T < 2.0$ GeV/c for Au + Au collisions at $\sqrt{s_{NN}}$ = 7.7, 19.6, and 200 GeV for different centrality selection methods. The third- and fourth-order cumulants from Fwd-All and Fwd-All-p centrality definitions at $\sqrt{s_{NN}}$ = 7.7 GeV are scaled with different factors to compare with other cases.
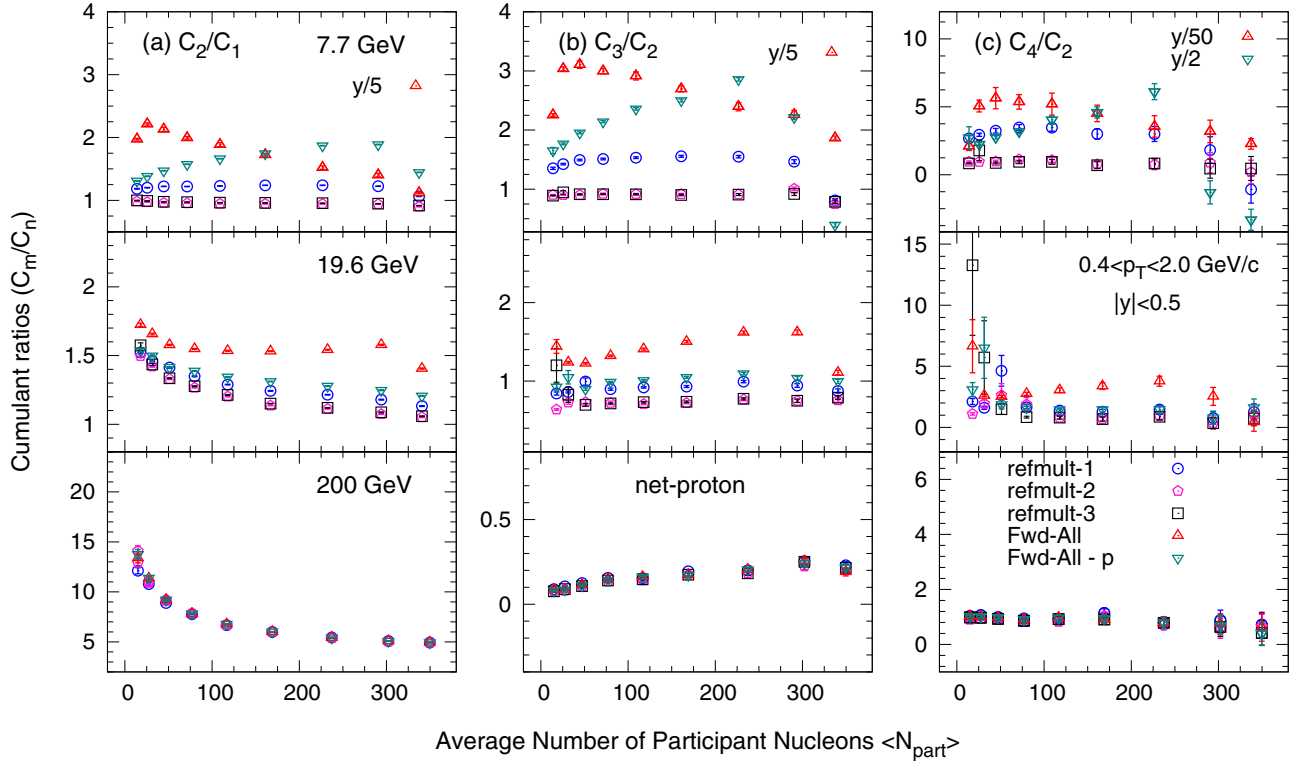
FIG. 9. Centrality dependence of cumulant ratios (C_2/C_1, C_3/C_2, and C_4/C_2) of net-proton multiplicity distributions within $|y| < 0.5$ and $0.4 < p_T < 2.0$ GeV/c for Au + Au collisions at $\sqrt{s_{NN}} = 7.7$, 19.6, and 200 GeV for different centrality selection methods. The second-, third-, and fourth-order cumulants from Fwd-All and Fwd-All-p centrality definitions at $\sqrt{s_{NN}} = 7.7$ GeV are scaled with different factors to compare with other cases.

refmult-3 centrality cases are smaller than the results from Fwd-All-p. We discuss this more later in the paper (Figs. 10–12), showing that this is due to better centrality resolution in the refmult-2 and refmult-3 cases than in the Fwd-All-p case and not caused by the autocorrelation effects in the refmult-2 and refmult-3 centrality definitions. At $\sqrt{s_{NN}} = 200$ GeV, the cumulants from the forward centrality definitions (Fwd-All and Fwd-All-p) are consistent with the results from the centralities defined at the central region (refmult-2 and "refmult-3). This comparison indicates that the autocorrelation effects in the centrality definitions of refmult-2 and refmult-3 are not significant within statistical uncertainties in Au + Au collisions at $\sqrt{s_{NN}} = 200$ GeV within UrQMD model calculations.

Figure 9 shows the $\langle N_{\text{part}} \rangle$ dependence of cumulant ratios [(a) $C_2/C_1 = \sigma^2/M$, (b) $C_3/C_2 = S\sigma$, and (c) $C_4/C_2 = \kappa\sigma^2$] of net-proton multiplicity distributions in Au + Au collisions at three different collision energies. At $\sqrt{s_{NN}} = 200$ GeV, all the cumulant ratios in different centrality selection sets are consistent with each other. As we go towards lower energies, the effect of centrality selection start to play an important role and cumulant ratios are deviating from each other. The results in centrality definition sets from the forward region show more deviates due to the poor centrality resolution caused by spectator proton contributions.

As shown in Figs. 8 and 9, the higher-order cumulants and cumulant ratios for the refmult-2 and refmult-3 centrality cases are smaller than the results from the forward region

centrality definition Fwd-All-p. We argue this is due to the better centrality resolution of the refmult-2 and refmult-3 centrality definitions than the case of Fwd-All-p. In Fig. 10, we show the charged-particle multiplicity distributions in various η windows in Au + Au collisions at $\sqrt{s_{NN}} = 19.6$
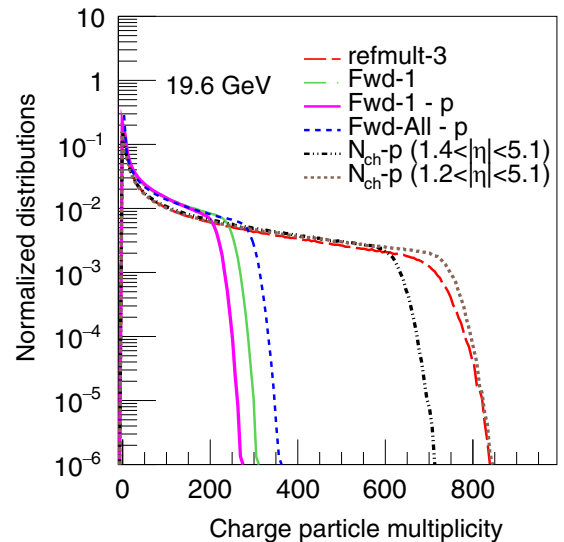

FIG. 10. Normalized distributions for charged-particle multiplicities in different η windows in Au + Au collisions at $\sqrt{s_{NN}} = 19.6$ from the UrQMD model.
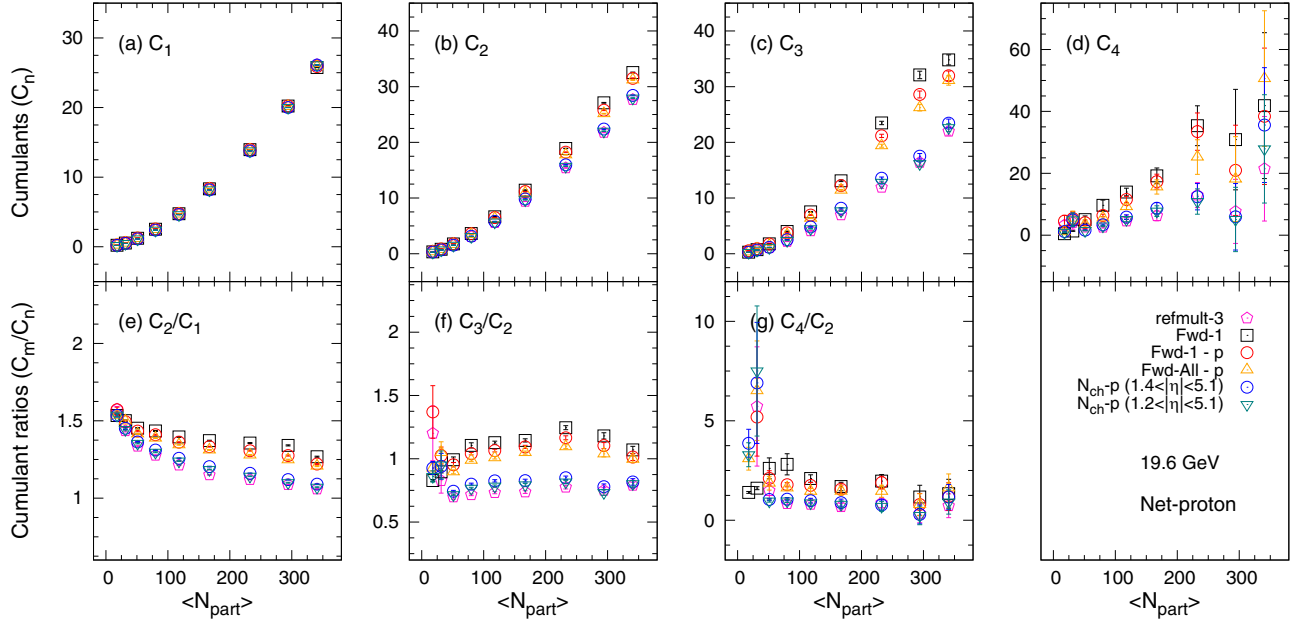
FIG. 11. Centrality dependence of cumulants (C_1–C_4) and cumulant ratios (C_2/C_1, C_3/C_2, and C_4/C_2) of net-proton multiplicity distributions within $|y| < 0.5$ and $0.4 < p_T < 2.0$ GeV/c in Au + Au collisions at $\sqrt{s_{NN}} = 19.6$ GeV for different centrality selection methods.

from the UrQMD model. We found that the charged-particle multiplicity from the refmult-3 centrality is much larger than that of the forward centrality definition Fwd-All-p. This will cause larger volume fluctuations with the Fwd-All-p centrality definition than the refmult-3 case. To justify this argument, two new centralities were defined for Au + Au collisions at $\sqrt{s_{NN}} = 19.6$ GeV from the UrQMD model with a wider η range in the forward region, which are charged-particle multiplicities (excluding protons) within $1.4 < |\eta| < 5.1$ and $1.2 < |\eta| < 5.1$. By doing this, the charged-particle multiplicities in the two new centrality definitions are much larger than those in the Fwd-All-p case and are similar to the multiplicities used in the refmult-3 centrality definition. In Fig. 11, the higher-order cumulant and cumulant ratios from the two new centralities are very close to each other with the results from the refmult-3 case and are much smaller than the Fwd-All-p centrality definition. It supports the argument that the large discrepancy between the results based on refmult-3 from the central region and Fwd-All-p from the forward region are originated from the poor centrality resolution of the Fwd-All-p definition. One may notice that there are small differences observed in C_2/C_1 and C_3/C_2 at noncentral Au + Au collisions between the refmult-3 and $N_{ch} - p$ ($1.2 < |\eta| < 5.1$) cases, which might be due to some remaining autocorrelation in the refmult-3 case. The comparison between the results of Fwd-1 and Fwd-1-p implies that the spectator protons have a wide η distribution in the forward region and can distort the centrality resolution even with a small fraction.

Figure 12 shows the energy dependence of the cumulant ratios (C_2/C_1, C_3/C_2, and C_4/C_2) of net-proton multiplicity distributions in Au + Au collisions at $\sqrt{s_{NN}} = 7.7$, 19.6, and 200 GeV for three centrality definition methods. The centrality-b is used to represent the centrality definition by using the impact parameter. The centrality bin width correction has been

applied to suppress volume fluctuations within wide centrality bins as discussed in Sec. III. For centrality-b, we first calculated cumulants in each 0.1-fm bin and then weighted the cumulants by the number of events in each 0.1-fm bin
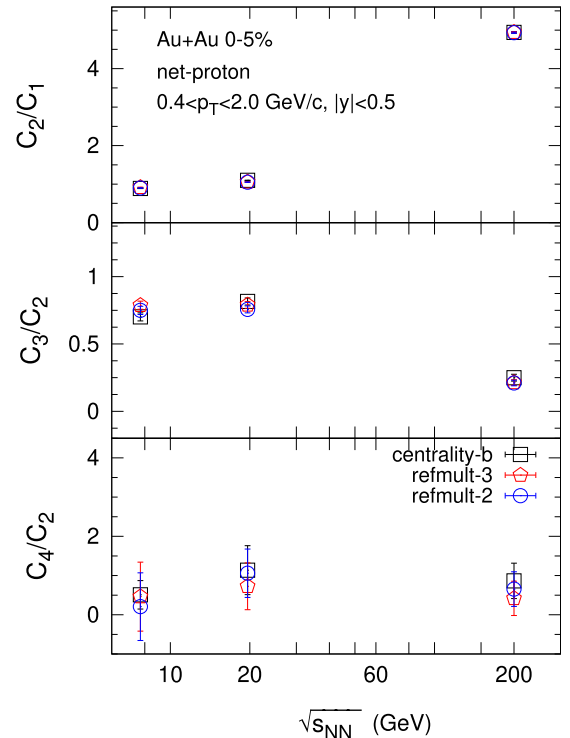

FIG. 12. Collision energy dependence of the cumulant ratios (C_2/C_1, C_3/C_2, and C_4/C_2) of net-proton multiplicity distributions within $|y| < 0.5$ and $0.4 < p_T < 2.0$ GeV/c in 0–5% most central Au + Au collisions for different centrality selection methods.

over a desired centrality class as discussed in Eq. (8). Based on the UrQMD model study, we found that the results in 0–5% most central Au + Au collisions from the refmult-3 and refmult-2 centralities are consistent with the results from the centrality-b definition, which is directly related to the initial collision geometry. This comparison further confirms that the refmult-3 and refmult-2 centrality definitions are robust to be used for studying the net-proton fluctuations in heavy-ion collisions.

VI. SUMMARY

The cumulants of net-proton multiplicity distributions are important observables to probe the signature of the QCD critical point in heavy-ion collisions. In this work, we studied the centrality dependence of cumulants (up to fourth order) and the cumulant ratios (C_2/C_1, C_3/C_2, and C_4/C_2) of net-proton multiplicity distributions at $\sqrt{s_{NN}} = 7.7$, 19.6, and 200 GeV for different centrality selection methods. These centralities were defined by the charged-particle multiplicities from different central or forward regions. We found that the mixture of the spectator protons and the produced charged particles can distort the centrality definition with charged-particle multiplicities at the forward region and worsen the centrality resolution. Particularly, the situation will be worse at lower energies, where most of the spectator protons will be detected by the STAR EPD. In the simulation, we demonstrated in detail that the centrality resolution can be significantly improved by excluding the spectator protons from the charged-particle multiplicity used for centrality definitions at the forward region. However, in the STAR experiment, the EPD does not have particle identification capability, and it would be very challenging to isolate these spectator protons from the produced charged particle and improve the centrality resolution. On the other hand, we found the higher-order cumulants calculated from the refmult-3 and refmult-2 centralities are consistent with the results from centralities defined by charged-particle multiplicities (excluding protons) at the forward region and the centrality-b. This means the suspected autocorrelation effects in the centrality definition of refmult-3 and refmult-2 at midrapidity are not significant within the statistical uncertainties within UrQMD model calculations. For the EPD centrality definition, one could use more differential information (η-segmented multiplicity within the EPD detector) and deep learning techniques [56]. Our work will serve as a baseline for the centrality selection of the fluctuation analysis in future relativistic heavy-ion collision experiments.

[1] M. M. Aggarwal *et al.* (STAR Collaboration), arXiv:1007.2613.
[2] K. Rajagopal, Nucl. Phys. A **661**, 150 (1999).
[3] M. A. Stephanov, PoS **LAT2006**, 024 (2006).
[4] E. S. Bowman and J. I. Kapusta, Phys. Rev. C **79**, 015202 (2009).
[5] Y. Aoki, G. Endrodi, Z. Fodor, S. D. Katz, and K. K. Szabo, Nature (London) **443**, 675 (2006).
[6] S. Gupta, X. Luo, B. Mohanty, H. G. Ritter, and N. Xu, Science **332**, 1525 (2011).
[7] Z. Fodor and S. D. Katz, J. High Energy Phys. 04 (2004) 050.
[8] P. de Forcrand and O. Philipsen, Nucl. Phys. B **642**, 290 (2002).
[9] S.-x. Qin, L. Chang, H. Chen, Y.-x. Liu, and C. D. Roberts, Phys. Rev. Lett. **106**, 172301 (2011).
[10] X.-Y. Xin, S.-X. Qin, and Y.-X. Liu, Phys. Rev. D **90**, 076006 (2014).
[11] C. Shi, Y.-L. Wang, Y. Jiang, Z.-F. Cui, and H.-S. Zong, J. High Energy Phys. 07 (2014) 014.
[12] C. S. Fischer, J. Luecker, and C. A. Welzbacher, Phys. Rev. D **90**, 034022 (2014).
[13] Y. Lu, Y.-L. Du, Z.-F. Cui, and H.-S. Zong, Eur. Phys. J. C **75**, 495 (2015).
[14] H. Zhang, D. Hou, T. Kojo, and B. Qin, Phys. Rev. D **96**, 114029 (2017).
[15] A. Bazavov, H. T. Ding, P. Hegde, O. Kaczmarek, F. Karsch, E. Laermann, S. Mukherjee, H. Ohno, P. Petreczky, E. Rinaldi, H. Sandmeyer, C. Schmidt, C. Schroeder, S. Sharma, W. Soeldner,

R. A. Soltz, P. Steinbrecher, and P. M. Vranas, Phys. Rev. D **96**, 074510 (2017).
[16] W.-j. Fu, J. M. Pawlowski, and F. Rennecke, arXiv:1909.02991.
[17] C. S. Fischer, Prog. Part. Nucl. Phys. **105**, 1 (2019).
[18] Z. Li, K. Xu, X. Wang, and M. Huang, Eur. Phys. J. C **79**, 245 (2019).
[19] X. Luo and N. Xu, Nucl. Sci. Tech. **28**, 112 (2017).
[20] M. A. Stephanov, K. Rajagopal, and E. V. Shuryak, Phys. Rev. Lett. **81**, 4816 (1998).
[21] A. Bzdak, S. Esumi, V. Koch, J. Liao, M. Stephanov, and N. Xu, arXiv:1906.00936.
[22] M. M. Aggarwal *et al.* (STAR Collaboration), Phys. Rev. Lett. **105**, 022302 (2010).
[23] L. Adamczyk *et al.* (STAR Collaboration), Phys. Rev. Lett. **112**, 032302 (2014).
[24] X. Luo, Nucl. Phys. A **956**, 75 (2016).
[25] J. Adam *et al.* (STAR Collaboration), arXiv:2001.02852.
[26] L. Adamczyk *et al.* (STAR Collaboration), Phys. Rev. Lett. **113**, 092301 (2014).
[27] L. Adamczyk *et al.* (STAR Collaboration), Phys. Lett. B **785**, 551 (2018).
[28] J. Adam *et al.* (STAR Collaboration), Phys. Rev. C **100**, 014902 (2019).
[29] M. A. Stephanov, Phys. Rev. Lett. **102**, 032301 (2009).
[30] M. A. Stephanov, Phys. Rev. Lett. **107**, 052301 (2011).
[31] X. Luo, J. Xu, B. Mohanty, and N. Xu, J. Phys. G: Nucl. Part. Phys. **40**, 105104 (2013).

[32] A. Chatterjee, S. Chatterjee, T. K. Nayak, and N. R. Sahoo, J. Phys. G: Nucl. Part. Phys. **43**, 125103 (2016).

[33] Y. Zhang, S. He, H. Liu, Z. Yang, and X. Luo, arXiv:1905.01095 [Phys. Rev. C (to be published)].

[34] G. D. Westfall, Phys. Rev. C **92**, 024902 (2015).

[35] M. Zhou and J. Jia, Phys. Rev. C **98**, 044903 (2018).

[36] J. Jia, C. Zhang, and J. Xu, arXiv:2001.08602.

[37] J. Adams *et al.*, arXiv:1912.05243.

[38] P. Shanmuganathan (STAR Collaboration), PoS **CPOD2017**, 066 (2018).

[39] S. A. Bass *et al.*, Prog. Part. Nucl. Phys. **41**, 255 (1998).

[40] M. Bleicher *et al.*, J. Phys. G: Nucl. Part. Phys. **25**, 1859 (1999).

[41] M. Bleicher, M. Belkacem, C. Ernst, H. Weber, L. Gerland, C. Spieles, S. A. Bass, H. Stoecker, and W. Greiner, Phys. Lett. B **435**, 9 (1998).

[42] M. Bleicher, S. Jeon, and V. Koch, Phys. Rev. C **62**, 061902(R) (2000).

[43] S. Haussler, H. Stöcker, and M. Bleicher, Phys. Rev. C **73**, 021901(R) (2006).

[44] N. R. Sahoo, S. De, and T. K. Nayak, Phys. Rev. C **87**, 044906 (2013).

[45] J. Xu, S. Yu, F. Liu, and X. Luo, Phys. Rev. C **94**, 024901 (2016).

[46] S. He and X. Luo, Phys. Lett. B **774**, 623 (2017).

[47] M. Mukherjee, S. Basu, A. Chatterjee, S. Chatterjee, S. P. Adhya, S. Thakur, and T. K. Nayak, Phys. Lett. B **784**, 1 (2018).

[48] C. Zhou, J. Xu, X. Luo, and F. Liu, Phys. Rev. C **96**, 014909 (2017).

[49] M. Kitazawa and X. Luo, Phys. Rev. C **96**, 024910 (2017).

[50] M. Cheng *et al.*, Phys. Rev. D **79**, 074505 (2009).

[51] B. I. Abelev *et al.* (STAR Collaboration), Phys. Rev. C **79**, 034909 (2009).

[52] M. L. Miller, K. Reygers, S. J. Sanders, and P. Steinberg, Annu. Rev. Nucl. Part. Sci. **57**, 205 (2007).

[53] M. Kendall and A. Stuart, *The Advanced Theory of Statistics*, (Griffin, London, 1943), Vol. 2.

[54] X. Luo, J. Phys. G: Nucl. Part. Phys. **39**, 025008 (2012).

[55] X. Luo, Phys. Rev. C **91**, 034907 (2015).

[56] Y. Sato, QM2019 poster, https://indico.cern.ch/event/792436/contributions/3533784

Correction: The name of a colleague was missing in the first sentence of the Acknowledgment section and has been set right.

Second Correction: The previously published Figs. 1, 3, and 4 contained minor plotting errors and have been replaced.

Third Correction: The previously published Figs. 5, 6, and 12 contained plotting errors and have been replaced.